IOP Publishing Physics in Medicine and Biology

Phys. Med. Biol. **58** (2013) 1269–1282 doi:10.1088/0031-9155/58/5/1269

Continuous depth-of-interaction measurement in a single-layer pixelated crystal array using a single-ended readout

Mikiko Ito[1], **Min Sun Lee**[1,2] **and Jae Sung Lee**[1,2,3,4,5]

[1] Department of Nuclear Medicine, Seoul National University, Seoul 110-744, Korea
[2] Interdisciplinary Programs in Radiation Applied Life Science, Seoul National University, Seoul 110-744, Korea
[3] Departments of Biomedical Sciences and WCU Brain and Cognitive Sciences, Seoul National University, Seoul 110-744, Korea
[4] Institute of Radiation Medicine, Medical Research Center, Seoul National University, Seoul 110-744, Korea

E-mail: jaes@snu.ac.kr

Received 15 September 2012, in final form 4 December 2012
Published 6 February 2013
Online at stacks.iop.org/PMB/58/1269

Abstract

We propose a depth-of-interaction (DOI)-encoding method to extract continuous DOI information using a single-layer scintillation crystal array with single-ended readout for cost-effective high-resolution positron emission tomography (PET). DOI information is estimated by different light dispersions along the *x*- and *y*-directions tailored by the geometric shape of reflectors around the crystals. The detector module comprised a 22 × 22 array of unpolished LGSO crystals (2.0 × 2.0 × 20 mm^3). A multi-anode photomultiplier tube with 64 anodes measured light dispersion in the crystal array. Gain non-uniformity of each anode was corrected by an analogue gain compensation circuit. DOI information was determined from peaks in the *x* and *y* anode-signal distributions normalized by the total energy of the distribution. Average DOI resolution (full width at half maximum, FWHM) over all crystals and depths was estimated to be 4.2 mm. Average energy resolution from the 2 to 18 mm DOI positions was 11.3% ± 0.79%, with 13% difference in photo-peak positions. Average time resolutions (FWHM) were 320–356 ps. Energy, time and DOI resolutions were uniform over all crystal positions except at the array's edge. This DOI-PET detector shows promise for applications that require high resolution and sensitivity at low cost.

(Some figures may appear in colour only in the online journal)

[5] Author to whom any correspondence should be addressed.

Introduction

A positron emission tomography (PET) detector with depth-of-interaction (DOI) capability allows PET scanners to achieve both high spatial resolution and high sensitivity (MacDonald and Dahlbom 1998, Jagoda *et al* 2004, Lee 2010, Ito *et al* 2011). Many DOI-encoding detectors have been developed for preclinical and organ-specific PET scanners. These PET scanners demand high spatial resolution and sensitivity mainly because of the small size of the imaging targets (Karp and Daube-Withespoon 1987, Worstell *et al* 2004, Murayama *et al* 1998, Levin 2000, Shao *et al* 2000, Liu *et al* 2001, Zhang *et al* 2002, Tsuda *et al* 2004, Yang *et al* 2006, Braem *et al* 2007, Du *et al* 2007, Jung e*t al* 2007, Hong e*t al* 2008, Ito *et al* 2010a, Vandenbroucke *et al* 2010, Freifelder and Karp 1997, Muehllehner 1976).

The DOI information is useful for reducing the parallax error that is caused by mispositioning a line of response at the peripheral field of view (FOV) of these preclinical and organ-specific PET scanners, which have a small-ring structure and narrow crystals. Reducing the parallax error enhances the spatial resolution of these scanners at the peripheral FOV while maintaining high sensitivity (Derenzo *et al* 1989, MacDonald and Dahlbom 1998, Moses 2001, Kim *et al* 2007, Visser *et al* 2009, Ito *et al* 2011). The improved spatial resolution at the peripheral FOV also allows the PET scanner to provide a larger fraction of useful FOV for the physical bore size.

Although many DOI-encoding PET detectors have been proposed, most have not yet translated into commercial systems mainly because of their cost (Lewellen 2008). This is because they require additional crystal arrays or photosensors to extract DOI information, which increases the number of crystals and photosensors required. Thus, recent efforts have focused on developing low-cost DOI-encoding detectors that do not require multiple crystal arrays or dual-ended readout (Lewellen 2010).

One of the most investigated low-cost DOI detectors is a monolithic-crystal PET detector in which the DOI information (in the z-direction) is estimated from the extent of light dispersion in a monolithic crystal slab (Cherry *et al* 1995, Delorme *et al* 1996, Joung *et al* 2002, Bruyndonckx *et al* 2003, 2007, Maas *et al* 2006, Ling *et al* 2007, van der Laan *et al* 2006, Schaart *et al* 2009, Vinke *et al* 2010). The location (in the x- and y-directions) of gamma-ray interactions in the crystal is calculated from the centroid (median point) of light dispersion. However, exact positioning of the gamma-ray events at the edge and corner of the crystal is still challenging because the light distribution is distorted at the side surfaces of the crystal owing to light reflection.

Another approach is to use a single-layer pixelated crystal array and a single-ended readout scheme. The use of a pixelated crystal array brings the advantage of easy identification of the gamma ray-interacted crystals by calculating and segmenting a flood histogram (x- and y-position map). Several designs for tailoring DOI dependence on light distribution or output pulse shape have been proposed to extract DOI information (i.e. cMiCE detector, phosphor-coated crystal detector, light crosstalk dispersion detector) (Miyaoka and Lewellen 1998, Lewellen *et al* 2002, Du *et al* 2009, Yang *et al* 2009).

We have proposed a novel PET detector concept to measure continuous DOI information in a single-layer crystal array using a single-ended readout (Ito *et al* 2010b). With this detector, DOI information (in the z-direction) can be extracted from the different light dispersion patterns along the x- and y-directions tailored by the geometric shape of the reflectors around the crystals, as shown in figure 1.

The aim of this study was to verify experimentally the concept of measuring DOI information and to investigate its performance. We built the detector block and then evaluated energy, time and DOI performances and its crystal identification capability.

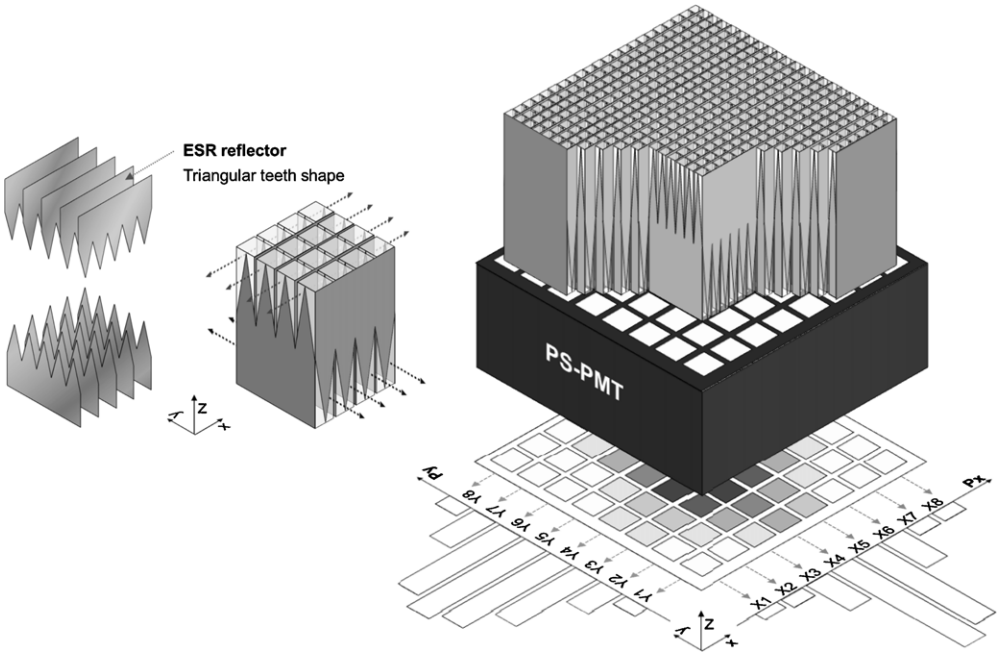

Figure 1. Proposed detector design. The crystals were inserted in the reflector grid created by crossing reflector strips in the shape of triangular teeth. Light dispersion was tailored by the shape of the reflectors around the crystals. Light spread in the *x*-direction in the upper half of the crystal array and in the *y*-direction in the lower half. The PMT anode signals were summed along the *x*- and *y*-directions, respectively.

Materials and methods

Detector module and experimental setup

We constructed the DOI-encoding detector using a single-layer (22 × 22) scintillation crystal array and a single-ended readout scheme. The crystal array consisted of rough (unpolished, or 'as cut') 2.0 × 2.0 × 20 mm^3 LGSO crystals ($Lu_{1.9}Gd_{0.1}SiO_5$:Ce; Hitachi Chemical, Tokyo, Japan). Each crystal was placed in a 3M enhanced specular reflector (ESR) grid that had been created by crossing the reflector strips in triangle-shaped teeth, as shown in figure 1. Because of the triangular teeth, the crystals were partially covered by the reflectors. Scintillation light can spread through the uncovered surface into the neighboring crystals. All but one of the outer surfaces of the crystal array were covered by ESR reflectors; the final surface was optically coupled to the entrance window of a flat-panel multianode photomultiplier tube (PMT) (H8500; Hamamatsu Photonics, Hamamatsu, Japan).

The H8500 PMT provides one dynode output and an 8 × 8 anode output array (Lee *et al* 2012). To reduce the number of output channels and correct any gain nonuniformity of individual anodes, the 64 anodes were connected to the resistor–matrix chain. This circuit sums up the anode signals along each anode row and column after gain correction to provide eight row-sum and eight column-sum analogue outputs (Popov *et al* 2006). These 16 output signals were digitalized and transferred to a personal computer through a VME module (V2718; CAEN, Viareggio, Italy). Using these 16 outputs, we measured the energy spectrum and light distribution for DOI- and crystal-position identification.

The dynode signal from H8500 PMT was used to generate the coincidence trigger signal with a reference detector and measure the timing properties. The reference detector—composed of a Hamamatsu fast PMT (R9800) and a polished LYSO crystal ($4.0 \times 4.0 \times 10$ mm^3) (SIPAT, Chongqing, China)—yielded a time resolution of 198 ps (Lee *et al* 2011, Ito *et al* 2012).

The anode signal of the reference detector and the dynode signal for testing the DOI-encoding detector were connected to a constant fraction discriminator (CFD) (model 935; ORTEC, Atlanta, GA, USA) with a 1.0 ns delay. Using the CFD output signals with the width of 20 ns, the coincidence trigger signals were generated by the Logic module (AND mode, model N455; CAEN), as shown in figure 2(a); the coincidence time window was 40 ns because of the width of the CFD output signals. The arrival times of CFD outputs were acquired by a time-to-digital converter (V775N; CAEN) with a common stop mode for timing a measurement.

'Front on' and 'side on' irradiation experiments

The flood histogram of the detector was measured by the 'front on' irradiation test setup. The reference detector and ^{22}Na radiation source were placed 40 cm away from the DOI detector for uniform irradiation of 511 keV gamma rays to all crystals in the DOI detector.

The 'side on' irradiation test, shown in figure 2(b), was performed to obtain individual performances at each depth in the crystals. Gamma rays emitted from the ^{22}Na source were collimated by two lead blocks and irradiated on the side of the crystal array. We changed the irradiation depth at 4 mm intervals (from the 2 mm to the 18 mm DOI positions) and measured energy and time properties and the DOI resolutions at these positions. While measuring the DOI-dependent performances, the other experimental conditions were fixed.

Crystal identification

For crystal identification of a whole crystal array in the detector, data were obtained by 'front-on' irradiation test setup. With this setup, we measured a flood map (two-dimensional histogram of the gamma-ray interaction position) integrated over all depths in the crystals. The flood map was calculated as the weighted mean by row-sum and column-sum signal distributions (P_y and P_x, respectively) as illustrated in figure 2(a).

Energy performance

Energy performances at each depth (2–18 mm at 4 mm intervals) were measured by 'side on' irradiation setup. Based on the flood map, depth-dependent energy performances were estimated at different crystal locations. The energy spectrum was calculated from the total of 16 output signals (8 row-sum and 8 column-sum signals) divided by 2; the total sum of the 16 signals is a double summation of all anode signals. We evaluated energy resolutions and energy peak positions (energy peak shift) as functions of the depth and crystal location. The energy peak shift as a function of depth can be used for energy calibration for better scatter rejection.

Time performance

Time performances as a function of the depth (2–18 mm at 4 mm intervals) were also measured by the 'side on' irradiation setup. Based on the crystal location information obtained from the flood map, we compared the time resolution and time walk as a function of the depth among

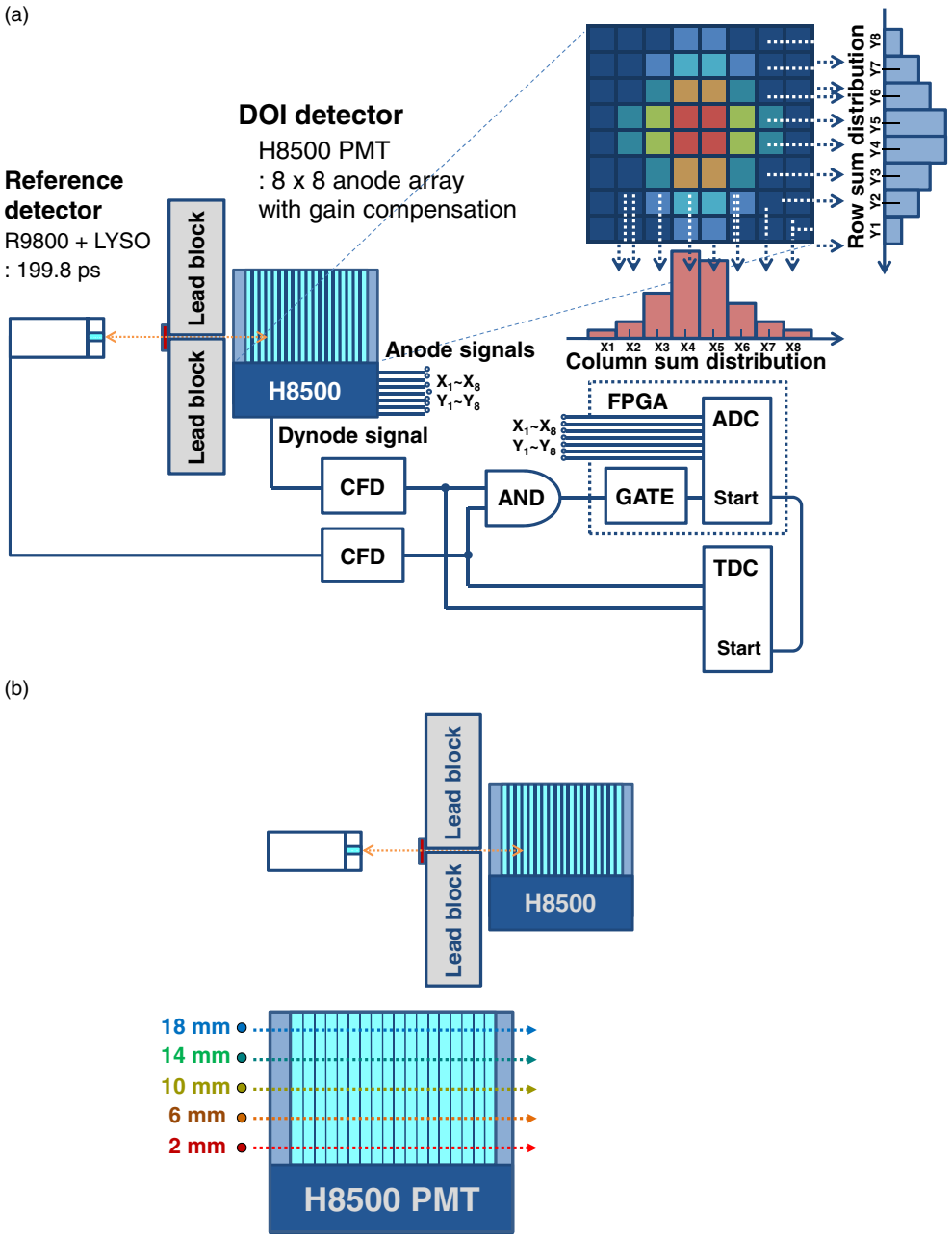

Figure 2. (a) Data acquisition setup to generate the coincidence trigger and to measure the energy, time and depth-of-interaction (DOI) performances as a function of the DOI position. PMT: photomultiplier tube; CFD: constant fraction discriminator; FPGA: field-programmable gate array; ADC: analogue-to digital converter; TDC: time-to-digital converter. (b) 'Side on' gamma-ray irradiation setup.

different crystal positions. Time spectrums were measured as the difference in arrival times between the DOI and reference detectors. The time resolution was calculated from the FWHM

of the time spectrum and corrected by the contribution of the reference time resolution to estimate single time resolution of the DOI detector. The time walk was calculated from the difference of the centroid in the time spectrums. The time walk information as a function of depth can be used for walk correction in post-processing.

DOI performance

DOI performance was also measured by 'side on' irradiation, and compared as a function of the crystal locations.

We estimated the DOI positions by comparing the P_x and P_y distributions. As shown in figure 1, scintillation light photons spread in different directions in the upper and lower halves of the crystal array. Also, the extent of light dispersion changes depended on the DOI position because of the triangular shape of the reflectors. Accordingly, the DOI position can be determined from the difference in light dispersions in the x- and y-directions. The P_x and P_y distributions were normalized by the energy (total output) of individual gamma-ray events. We determined DOI positions from the difference in peak amplitudes ($\mathrm{DOI} = a_x - A \cdot a_y$) between the P_x and P_y distributions normalized by the energy (where A is a constant). The a_x and a_y are the peak amplitudes of the raw signal distributions (P_x and P_y) devised by the energy of each event; we did not use curve fitting to extract the peak amplitudes. The constant A was determined from the slope of a_x versus a_y graph (2D-plot); we used the same constant A ($A = 2.5$) for the calculation of DOI at all different crystal locations. We did so because this DOI index, which is based on peak values of light distributions, yielded the best DOI resolution.

Results

Crystal identification

The relative advantage of using a pixelated crystal array instead of a monolithic crystal slab is simple crystal identification on a flood map. The flood map was generated by calculating the x- and y-positions of each gamma-ray interaction with the crystals with 'front-on' irradiation (figure 3(a)). Each x- and y-position was estimated as the weighted mean by P_x and P_y, respectively. The flood map revealed that the crystals were well resolved, except those located at the edge of the crystal array. The two neighboring edge crystals, however, can be resolved in the flood maps obtained by 'side-on' irradiation at each DOI position (figure 3(b)). Figure 3(b) also shows that the centers of two crystal positions shift inside the map as the DOI position increases. The depth-dependent shift of crystal position at the edge of the crystal array is in accord with the results of a Monte Carlo simulation conducted in our previous study (Ito *et al* 2010b).

Energy properties

The energy and time properties of the DOI detector were measured by 'side-on' gamma-ray irradiation. As previously described, we measured these properties according to the DOI position while we adjusted the 'side-on' irradiation depth to various points between 2 and 18 mm.

Figure 4 shows the energy spectra measured at different DOI positions (gamma ray irradiation depths), which were obtained at the center crystal of the array. Figure 5 shows the energy resolution (figure 5(a)) and photo-peak position (figure 5(b)) as a function of the DOI position. The uniform energy resolution values along the DOI positions yielded an average energy resolution of $11.3\% \pm 0.79\%$. Figure 5(b) shows that the photo-peak

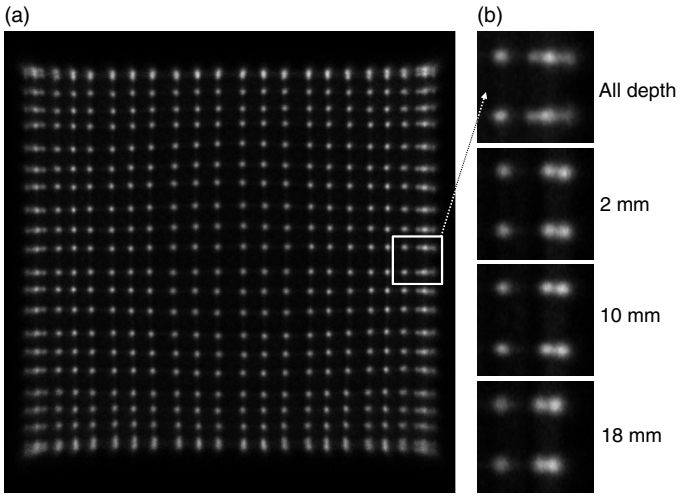

Figure 3. The flood histogram for crystal identification. The crystal array (22 × 22 array of 2.0 × 2.0 × 20 mm^3 crystals) was exposed to gamma rays irradiated to the front and side of the crystal array. (a) 'Front on' gamma-ray irradiation. (b) Comparison of flood images at the edge region (white line square) between 'front on' (all depth) and 'side on' gamma-ray irradiation at the 2, 10 and 18 mm DOI positions. Only the area indicated by the outlined square in (a) was magnified (b).

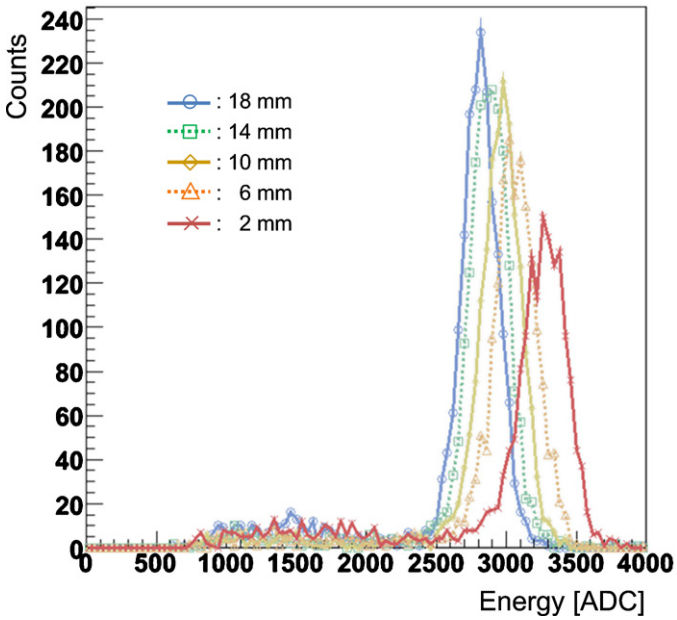

Figure 4. Energy distributions at the center of the crystal array at DOI positions 2–18 mm. The *x*-axis was the arbitrary ADC output value.

position becomes lower as the DOI position is farther from the PMT surface. The difference in photo-peak between the 2 and 18 mm DOI positions was approximately 13%. This difference indicates that energy calibration using the DOI information can be useful for better scatter rejection in PET systems that incorporate this DOI detector.

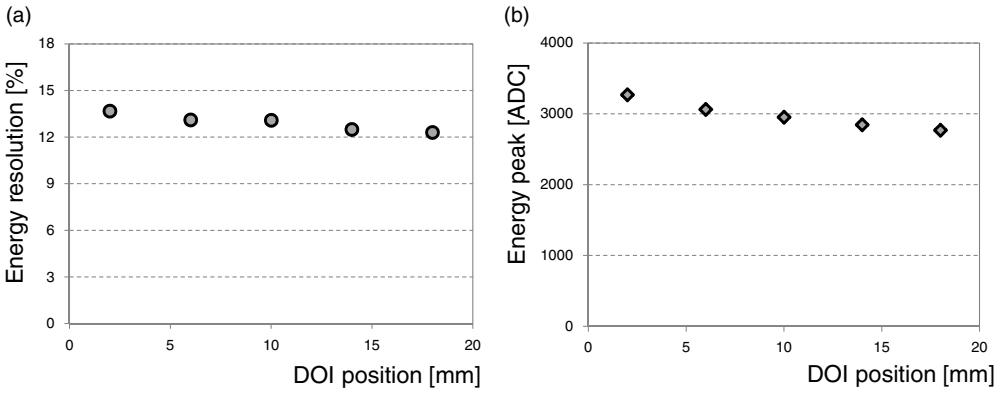

Figure 5. Energy performance at the center of the crystal array as a function of the DOI position. Energy resolution (a) and energy peak (b) mean values measured while moving the gamma-ray irradiation position from the 2 mm to the 18 mm DOI position.

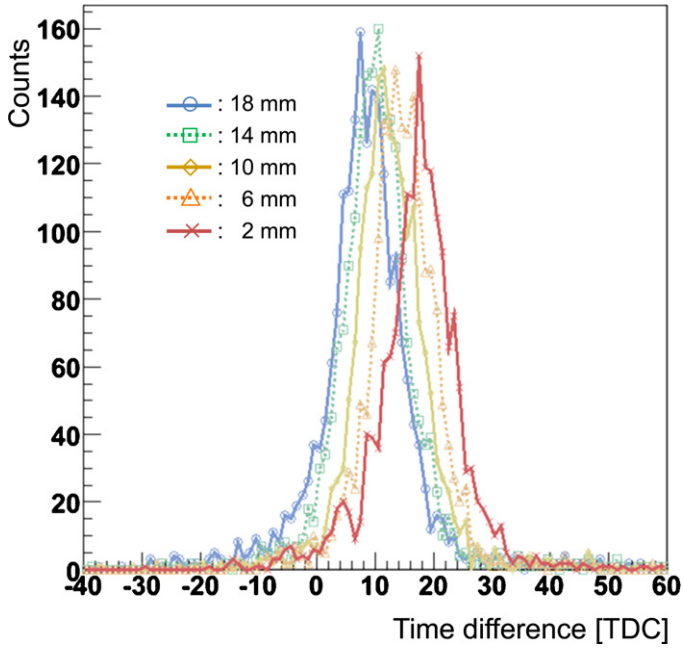

Figure 6. Coincidence time distributions at the center of the crystal array at various DOI positions The *x*-axis is the arbitrary TDC output value.

Time properties

Figure 6 shows the distribution of the coincidence time difference (Δt) measured at different DOI positions and at the center crystal. Figure 7 shows the (single) time resolution (figure 7(a)) and centroid (figure 7(b)) of the Δt distribution (figure 6) as a function of the DOI position. The time resolutions were calculated as the full width at half maximum (FWHM) of the Δt distribution and corrected for the contribution of the timing uncertainty of the reference detector (198 ps). Generally, better time resolution was obtained at DOI positions closer to the PMT surface (320 ps at 2 mm versus. 356 ps at 18 mm). Figure 7(b) shows that the centroid of the Δt distribution shifts as the DOI position changes. The shift of the centroid

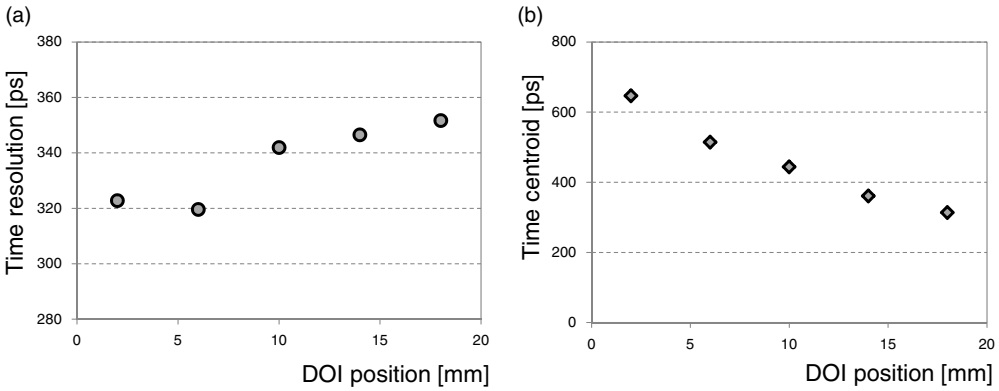

Figure 7. Time performance at the center of the crystal array as a function of the DOI position. (a) Single time resolution (full width at half maximum, or FWHM) and (b) centroid positions in the coincidence time distribution measured while moving the gamma-ray irradiation point from the 2 to the 18 mm DOI position. The single time resolutions were corrected by the contribution of the reference time resolution (198 ps).

indicates generation of a 'time walk' (difference in light transport time) was caused by the different DOI positions as the distance between the irradiation source and the target was fixed in this experiment. The time walk between the 2 and 18 mm DOI positions was approximately 340 ps.

Figure 8 shows the energy and time resolutions as a function of the DOI position and crystal location. These performances were generally uniform along the crystals located from the center to the edge of the array but were slightly degraded at the edge of the crystal.

DOI identification

The DOI information was derived from the difference in light distribution along the x- and y-directions inside the crystal array. Figure 9 shows P_x and P_y distributions, which were normalized by the total sum of the signals. These average signal distributions (figure 9) were measured at the center of the crystal array (11th crystal in x-direction and 12th in y-direction). Note that the P_x and P_y distributions changed differently as the DOI position changed. As the DOI position became farther away from the PMT surface (from 2 to 18 mm) the peak height of the P_x distribution decreased, whereas the P_y distribution showed a change in the opposite direction (increased peak height). Therefore, we used the DOI index that reflects the difference between the peak heights of the P_x and P_y distributions (maximums of raw-signals); we did not use any curve fitting to estimate peak positions.

Figure 10 shows the DOI index distributions measured at the center crystal of the array. The red, orange, yellow, green and blue lines in figure 10 correspond to each DOI position (from 2 to 18 mm at 4 mm intervals away from the PMT surface). The average DOI resolution was 4.3 mm, which was calculated as the FWHM of each DOI index distribution, each of which was calibrated by the distance between the peaks (Ito *et al* 2010b).

Figure 11 shows the DOI response as a function of the DOI position and crystal location. The circles and error bars indicate the centroid and the FWHM of the DOI index distributions, respectively. These plots of the DOI index as a function of the DOI position have a repeatable sawtooth pattern (four bumps). The pattern exactly matches the gaps between the anode cells in the H8500, indicating bias for estimations of the peak values (a_x and a_y) for crystals above these gaps.

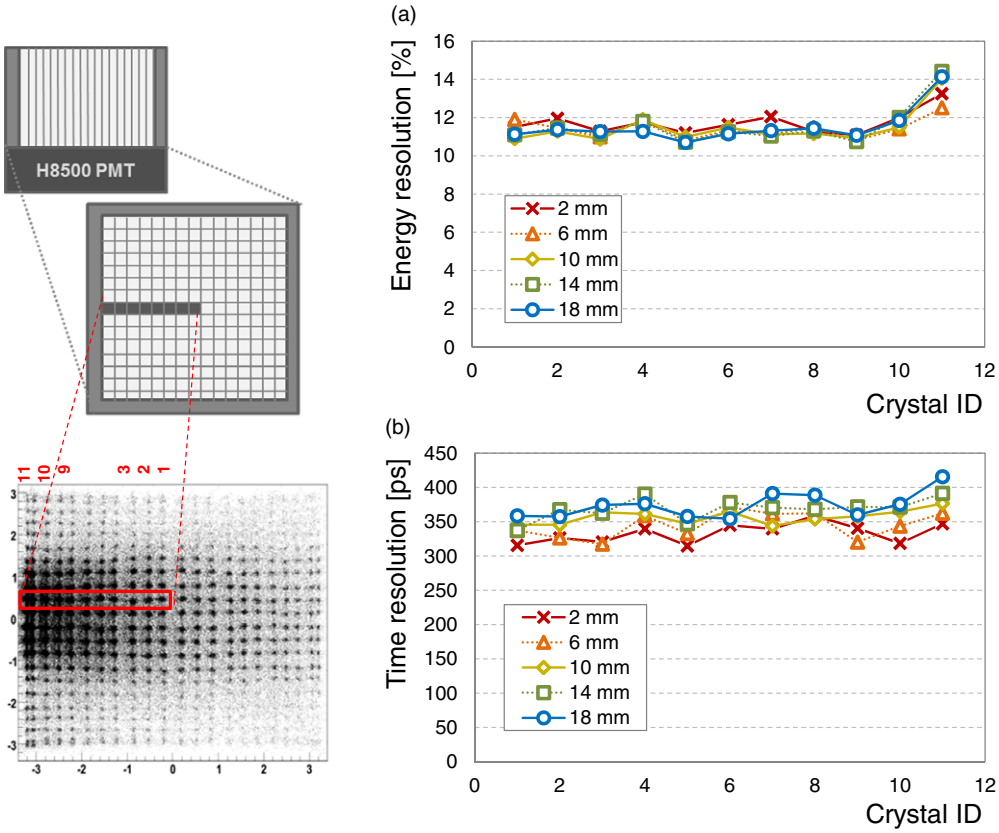

Figure 8. Crystal location dependence on energy and time performance. Energy resolutions (a) and single time resolutions (FWHM) (b) as a function of the DOI position are presented for various crystal locations (crystal ID 1–11).

Discussion

In this novel DOI detector, we employed unpolished LGSO crystals to enable light dispersion between neighboring crystals through the rough crystal surface not covered by reflectors. The use of unpolished crystals yields more scatter of scintillation light photons and longer pathways of light transport to the PMT surface than polished crystals because the scintillation light is diffused on the rough surface of crystal. The increased scatter and longer transport lead to more light attenuation, which causes the photo-peak in the energy spectrum to decrease as the distance between the DOI position and the PMT surface increases (figure 5(b)). In addition, the time walk between the 2 and 18 mm DOI positions was estimated to be relatively longer (340 ps) than when polished crystals were used (100–200 ps) (Shibuya *et al* 2008, Vinke *et al* 2010, Spanoudaki and Levin 2011). This time walk information as a function of DOI position can be utilized for elevating the timing performance of this detector at the system level as the time resolution at each DOI position ranges from 320 to 356 ps (Ito *et al* 2011).

In the previous study using Monte Carlo simulation (Ito *et al* 2010b), we determined the DOI position based on the variances of x- and y-signal distributions (P_x and P_y). Meanwhile, in this study, we used the difference in peak amplitudes of P_x and P_y because of its simplicity in the real-time calculation of DOI that will be needed in the future implementation of this method.

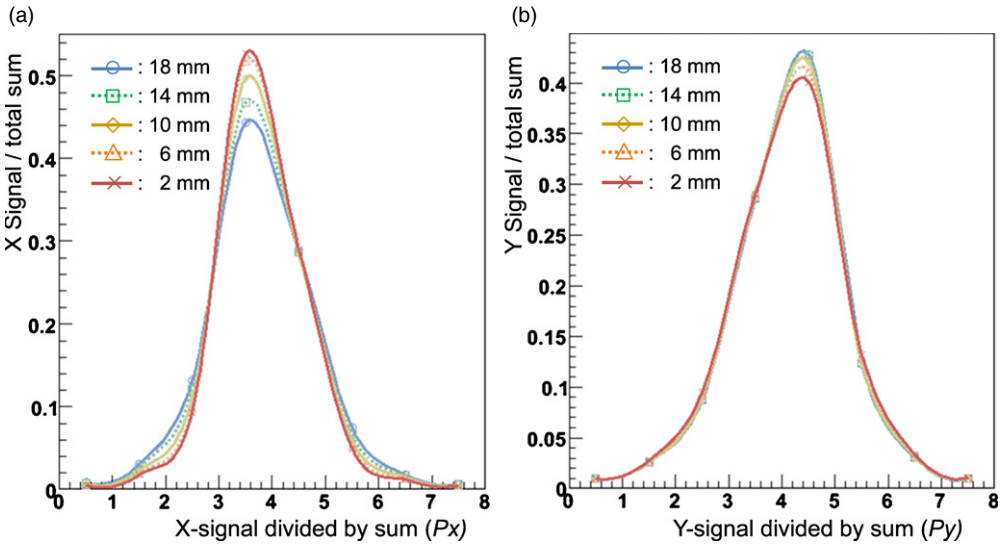

Figure 9. Signal distribution change according to the DOI position. The P_x (a) and P_y (b) distributions normalized by the total sum of the signals (sum P_x or P_y) for individual events. The signal distributions changed with the change in DOI position. Note that the change pattern was different for P_x and P_y.

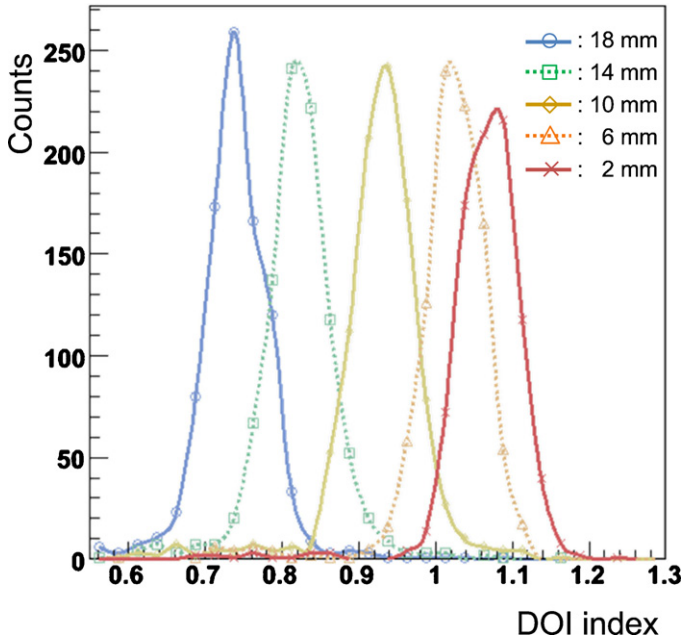

Figure 10. DOI distribution (at the center of the crystal array) calculated from the difference in signal peaks between the row-signal and column-signal distributions normalized by energy.

Although the length of the triangular teeth was not different in the upper and lower halves of the crystal array (the same reflector grids were symmetrically arranged in the *x*- and *y*-directions), the DOI-dependent amplitude change in normalized P_y distributions (figure 9(b))

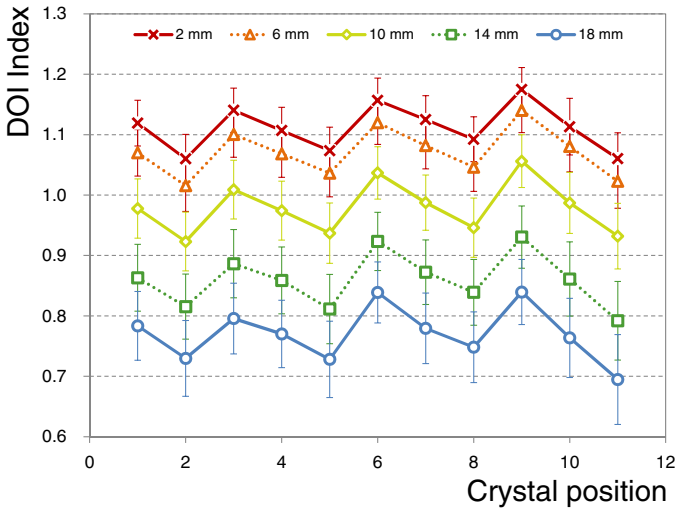

Figure 11. DOI performance obtained at various crystal locations. The data plots and error bars indicate the DOI mean values and the FWHMs of the DOI distribution for each DOI position.

was relatively smaller than that in normalized P_x distributions (figure 9(a)). The difference is because the two major factors that determine light dispersion (teeth width and transport path length) act cooperatively in the x-direction but not in the y-direction. In the x-direction, light dispersion tailored by the reflector shape increases as the distance between the DOI position and the PMT surface increases. The light dispersion due to longer transportation from the DOI position to the PMT surface also increases as the distance increases. On the other hand, the triangular teeth in y-direction headed to PMT surface, making larger light dispersion as DOI position is closer to the PMT. The opposite effects between light dispersions by the reflector shape and by the light transportation would hinder the DOI-dependent amplitude change in the P_y distribution.

The peak amplitudes of the P_x and P_y distributions were used to calculate the DOI index. The pitch of sensitive pixels in the H8500 PMT (6×6 mm^2) is approximately three times larger than the cross section of the crystal used in this study (2×2 mm^2). We expect that the photo-sensors with smaller pixel size (e.g., H9500 PMT or silicon photomultiplier arrays; Yamamoto *et al* 2011, Yoon *et al* 2012) provide more accurate light distribution estimations, improving DOI resolution.

Summary and conclusion

We developed a prototype DOI PET detector module composed of a single-layer pixelated crystal array and single-ended readout scheme to attain high spatial resolution and sensitivity. Our ultimate goal was to apply it to small animal and specific organ imaging at relatively low cost. In contrast to other well-known low-cost detectors based on a monolithic crystal slab, this continuous DOI detector with its pixelated crystal array enables simple crystal identification using a flood histogram. Uniform energy resolution of 11.3% $\pm$ 0.79% was obtained from the 2 to the 18 mm DOI position. Timing resolution was excellent but depended on the DOI position, the time ranging from 320 to 356 ps. Average DOI resolution was estimated to be 4.2 mm. All the energy, time and DOI performances were uniform along the crystals located

from the center to the edge of the crystal array but were slightly degraded at the edge of the crystal. We concluded that the prototype continuous DOI PET detector shows promise for applications that require high resolution and sensitivity.

Acknowledgments

This work was supported by grants from the Atomic Energy R&D Program (2008-2003852, 2010-0026012) and the WCU Program (R31-10089) through the KOSEF funded by the Korean Ministry of Education, Science, and Technology.

References

Braem A *et al* 2007 High precision axial coordinate readout for an axial 3D PET detector module using a wavelength shifter strip matrix *Nucl. Instrum. Methods* A **580** 1513–21

Bruyndonckx P, Lemaître C, Schaart D, Maas M, van der Laan D J, Krieguer M, Devroede O and Tavernier S 2007 Towards a continuous crystal APD-based PET detector design *Nucl. Instrum. Methods* A **571** 182–6

Bruyndonckx P, Leonard S, Liu J, Tavernier S, Szupryczynski P and Fedorov A 2003 Study of spatial resolution and depth of interaction of APD-based PET detector modules using light sharing schemes *IEEE Trans. Nucl. Sci.* **50** 1415–19

Cherry S R, Shao Y, Tornai M P, Siegel S, Ricci A R and Phelps M E 1995 Collection of scintillation light from small BGO crystals *IEEE Trans. Nucl. Sci.* **42** 1058–63

Delorme S, Frei R, Joseph C, Loude J-F and Morel C 1996 Use of a neural network to exploit light division in a triangular scintillating crystal *Nucl. Instrum. Methods* A **373** 111–8

Derenzo S E, Moses W W, Jackson H G, Turko B T, Cahoon J L, Geyer A B and Vuletich T 1989 Initial characterization of a position-sensitive photodiode/BGO detector for PET *IEEE Trans. Nucl. Sci.* **36** 1084–9

Du H, Yang Y and Cherry S R 2007 Measurements of wavelength shifting (WLS) fibre readout for a highly multiplexed, depth-encoding PET detector *Phys. Med. Biol.* **52** 2499–514

Du H, Yang Y, Glodo J, Wu Y, Shah K and Cherry S R 2009 Continuous depth-of-interaction encoding using phosphor-coated scintillators *Phys. Med. Biol.* **54** 1757–71

Freifelder R and Karp J S 1997 Dedicated PET scanners for breast imaging *Phys. Med. Biol.* **42** 2463–80

Hong S J, Kwon S I, Ito M, Lee G S, Sim K S, Park K S, Rhee J T and Lee J S 2008 Concept verification of three-layer DOI detectors for animal PET *IEEE Trans. Nucl. Sci.* **55** 912–7

Ito M, Hong S J and Lee J S 2011 Positron emission tomography (PET) detectors with depth-of- interaction (DOI) capability *Biomed. Eng. Lett.* **1** 70–81

Ito M, Lee J P and Lee J S 2012 Timing performance study of new fast PMTs with LYSO for time-of-flight PET *IEEE Trans. Nucl. Sci.* at press (doi:10.1109/TNS.2012.2215342)

Ito M, Lee J S, Kwon S I, Lee G S, Hong B, Lee K S, Sim K S, Lee S J, Rhee J T and Hong S J 2010a A four-layer DOI detector with a relative offset for use in an animal PET system *IEEE Trans. Nucl. Sci.* **57** 976–82

Ito M, Lee J S, Park M J, Sim K S and Hong S J 2010b Design and simulation of a novel method for determining depth-of-interaction in a PET scintillation crystal array using a single-ended readout by a multi-anode PMT *Phys. Med. Biol.* **55** 3827–41

Jagoda E M, Vaquero J J, Seidel J, Green M V and Eckelman W C 2004 Experiment assessment of mass effects in the rat: implications for small animal PET imaging *Nucl. Med. Biol.* **31** 771–9

Joung J, Miyaoka R S and Lewellen T K 2002 cMiCE: a high resolution animal PET using continuous LSO with a statistics based positioning scheme *Nucl. Instrum. Methods* A **489** 584–98

Jung J H, Choi Y, Chung Y H, Devroede O, Krieguer M, Bruyndonckx P and Tavernier S 2007 Optimization of LSO/LuYAP phoswich detector for small animal PET *Nucl. Instrum. Methods* A **571** 669–75

Karp J S and Daube-Withespoon M E 1987 Depth-of-interaction determination in NaI(TI) and BGO scintillation crystals using a temperature gradient *Nucl. Instrum. Methods* A **260** 509–17

Kim J S, Lee J S, Im K C, Kim S J, Kim S Y, Lee D S and Moon D H 2007 Performance measurement of the microPET Focus 120 scanner *J. Nucl. Med.* **48** 1527–35

Lee C M, Kwon S I, Ko G B, Ito M, Yoon H S, Lee D S, Hong S J and Lee J S 2012 A novel compensation method for the anode gain non-uniformity of multi-anode photomultiplier tubes *Phys. Med. Biol.* **57** 191–207

Lee J P, Ito M and Lee J S 2011 Evaluation of a fast photomultiplier tube for time-of-flight PET *Biomed. Eng. Lett.* **1** 174–9

Lee J S 2010 Technical advances in current PET and hybrid imaging systems *Open Nucl. Med. J.* **2** 192–208

Levin C S 2000 Design of a high-resolution and high-sensitivity scintillation crystal array for PET with nearly complete light collection *IEEE Trans. Nucl. Sci.* **49** 2236–43

Lewellen T K 2008 Recent developments in PET detector technology *Phys. Med. Biol.* **53** 287–317b

Lewellen T K 2010 The challenge of detector designs for PET *AJR Am. J. Roentgenol.* **195** 301–9

Lewellen T K, Janes M and Miyaoka R S 2002 DMice-a depth-of-interaction detector design for PET scanners *IEEE Nucl. Sci. Symp. Conf. Rec.* pp 2288–92

Ling T, Lewellen T K and Miyaoka R S 2007 Depth of interaction decoding of a continuous crystal detector module *Phys. Med. Biol.* **52** 2213–28

Liu H, Omura T, Watanabe M and Yamashita T 2001 Development of a depth of interaction detector for gamma-rays *Nucl. Instrum. Methods* A **459** 182–90

Maas M C, van der Laan D J, Schaart D R, Huizenga J, Brouwer J C, Bruyndonckx P, Leonard S, Lemaitre C and van Eijk C W E 2006 Experimental characterization of monolithic-crystal small animal PET detectors read out by APD arrays *IEEE Trans. Nucl. Sci.* **53** 1071–7

MacDonald L R and Dahlbom M 1998 Parallax correction in PET using depth of interaction information *IEEE Trans. Nucl. Sci.* **45** 2232–7

Miyaoka R S and Lewellen T K 1998 Design of a depth of interaction (DOI) PET detector module *IEEE Trans. Nucl. Sci.* **45** 1069–73

Moses W W 2001 Trends in PET imaging *Nucl. Instrum. Methods* A **471** 209–14

Muehllehner G 1976 Resolution limit of positron cameras *J. Nucl. Med.* **17** 757–8

Murayama H, Ishibashi I, Uchida H, Omura T and Yamashita T 1998 Depth encoding multicrystal detectors for PET *IEEE Trans. Nucl. Sci.* **45** 1152–8

Popov V, Majewski S and Welch B L 2006 A novel readout concept for multianode photomultiplier tubes with pad matrix anode layout *Nucl. Instrum. Methods* A **567** 319–22

Schaart D R, van Dam H T, Seifert S, Vinke R, Dendooven P, Löhner H and Beekman F J 2009 A novel, SiPM-array-based, monolithic scintillator detector for PET *Phys. Med. Biol.* **54** 3501–12

Shao Y, Silverman R W, Farrell R, Cirignano L, Grazioso R, Shah K S, Vissel G, Clajus M, Tumer T O and Cherry S R 2000 Design studies of a high resolution PET detector using APD arrays *IEEE Trans. Nucl. Sci.* **47** 1051–7

Shibuya K, Nishikido F, Tsuda T, Kobayashi T, Lam C, Yamaya T, Yoshida E, Inadama N and Murayama H 2008 Timing resolution improved by DOI information in an LYSO TOF-PET detector *Nucl. Instrum. Methods* A **593** 572–7

Spanoudaki V C and Levin C S 2011 Investigating the temporal resolution limits of scintillation detection from pixelated elements: comparison between experiment and simulation *Phys. Med. Biol.* **56** 735–56

Tsuda T, Murayama H, Kitamura K, Yamaya T, Yoshida E, Omura T, Kawai H, Inadama N and Orita N 2004 A four-layer depth of interaction detector block for small animal PET *IEEE Trans. Nucl. Sci.* **51** 2537–42

Vandenbroucke A, Foudray A M, Olcott P D and Levin C S 2010 Performance characterization of a new high resolution PET scintillation detector *Phys. Med. Biol.* **55** 5895–911

van der Laan D J, Maas M C, Schaart D R, Bruyndonckx P, Lamaitre C and van Eijk C W E 2006 Spatial resolution in positionsensitive monolithic scintillation detectors *IEEE Nucl. Sci. Symp. Conf. Rec.* pp 2506–10

Vinke R, Löhner H, Schaart D R, van Dam H T, Seifert S, Beekman F J and Dendooven P 2010 Time walk correction for TOF-PET detectors based on a monolithic scintillation crystal coupled to a photosensor array *Nucl. Instrum. Methods* A **621** 595–604

Visser E P, Disselhorst J A, Brom M, Laverman P, Gotthardt M, Oyen W J and Boerman O C 2009 Spatial resolution and sensitivity of the Inveon small-animal PET scanner *J. Nucl. Med.* **50** 139–47

Worstell W *et al* 2004 Design and performance of a prototype whole-body PET/CT scanner with fiber optic readout *IEEE Nucl. Sci. Symp. Conf. Rec.* pp 3280–4

Yamamoto S, Watabe H and Hatazawa J 2011 Performance comparison of Si-PM-based block detectors with different pixel sizes for an ultrahigh-resolution small-animal PET system *Phys. Med. Biol.* **56** N227–36

Yang Y, Dokhale P A, Silverman R W, Shah K S, McClish M A, Farrell R, Entine G and Cherry S R 2006 Depth of interaction resolution measurements for a high resolution PET detector using position sensitive avalanche photodiodes *Phys. Med. Biol.* **51** 2131–42

Yang Y, Wu Y and Cherry S R 2009 Investigation of depth of interaction encoding for a pixelated LSO array with a single multi-channel PMT *IEEE Trans. Nucl. Sci.* **56** 2594–9

Yoon H S, Ko G B, Kwon S I, Lee C M, Ito M, Chan Song I, Lee D S, Hong S J and Lee J S 2012 Initial results of simultaneous PET/MRI experiments with an MRI-compatible silicon photomultiplier PET scanner *J. Nucl. Med.* **53** 608–14

Zhang N, Thompson C J, Togane D, Cayouette F and Nguyen K Q 2002 Anode position and last dynode timing circuits for dual-layer BGO scintillator with PS-PMT based modular PET detectors *IEEE Trans. Nucl. Sci.* **49** 2203–7